

Full-Head Segmentation of MRI with Abnormal Brain Anatomy: Model and Data Release

Andrew M Birnbaum, Adam Buchwald, Peter Turkeltaub, Adam Jacks,

Yu Huang, Abhishek Datta, Lucas C Parra, Lukas A Hirsch

Abstract - The goal of this work was to develop a deep network for whole-head segmentation including clinical MRIs with abnormal anatomy, and compile the first public benchmark dataset for this purpose. We collected 91 MRIs with volumetric segmentation labels for a diverse set of human subjects (4 normal, 32 traumatic brain injuries, 57 strokes). These clinical cases are characterized by extended cerebro-spinal fluid in regions normally containing the brain. Training labels were generated by manually correcting initial automated segmentations for skin/scalp, skull, CSF, gray matter, white matter, air cavity and extracerebral air. We developed a “MultiAxial” network consisting of three 2D U-Net that operate independently in sagittal, axial and coronal planes and are then combined to produce a single 3D segmentation. The MultiAxial network achieved a test-set Dice scores of 0.88 ± 0.04 (median \pm interquartile range). For brain tissue, it significantly outperforms existing brain segmentation methods (MultiAxial: 0.898 ± 0.041 , SynthSeg: 0.758 ± 0.054 , BrianChop: 0.757 ± 0.125). The MultiAxial network gains in robustness by avoiding the need for coregistration with an atlas. It performed well in regions with abnormal anatomy and on images that have been de-identified. It enables more robust current flow modeling when incorporated into ROAST, a widely-used modeling toolbox for transcranial electric stimulation. We are releasing a state-of-the-art model for whole-head MRI segmentation, along with a dataset of 61 clinical MRIs and training labels including non-brain structures. Together the model and data may serve as a benchmark for future efforts.

Index Terms—Magnetic Resonance Imaging, Convolutional Neural Network, Segmentation

A. M. Birnbaum, Y. Huang, L. C. Parra, and L. A. Hirsch are with the Department of Biomedical Engineering, The City College of New York, New York, NY 10031 USA (e-mails: birnbaumandrew@gmail.com, andypotato@gmail.com, parra@ccny.cuny.edu, lukashirsch@gmail.com). A. Datta is with Soterix Medical, New York, NY, USA (e-mail: abdatta@gmail.com). A. Buchwald is with New York University, New York, NY, USA (e-mail: buchwald@nyu.edu). P. Turkeltaub is with the Department of Neurology, Georgetown University, Washington, DC, USA (e-mail: turkelt@georgetown.edu). A. Jacks is with the Department of Allied Health Sciences, University of North Carolina School of Medicine, Chapel Hill, NC, USA (e-mail: adam_jacks@med.unc.edu).

I. INTRODUCTION

Magnetic Resonance Imaging (MRI) of the brain is used extensively in clinical practice, in medical research and in neuroscience. Volumetric assessment of brain anatomy plays an important role in these areas. In a clinic, measuring the extent of a tumor is important for planning of surgery and radiation therapy[1] as well as monitoring of tumor progression and treatment response[2]. Measuring brain volume is important also

in diagnosis of conditions such as Alzheimer's disease[3], traumatic brain injury[4], hydrocephalus[5] and stroke[6]. Measuring brain volume implies delineating cerebro-spinal fluid (CSF), which fills up the space left behind by a deteriorating brain. In chronic stroke in particular, the lesioned brain tissue is cleared up and the space is filled in with CSF in as little as 6 months from the injury[7]. In neuroscience, measuring the volume of gray and white matter in different brain areas also plays an important role in explaining brain function[8]. Finally, the idiosyncratic differences in anatomy across individuals can have large effects on encephalographic brain signals[9] and transcranial brain stimulation[10]. Therefore current flow modeling, as used in ROAST[11], [12], Brainstorm[13], and SimNIBS[14], all required accurate automatic segmentation of the human head. Yet, existing tools are largely limited to brain segmentation, and fail for clinical cases with abnormal anatomy. For all these use cases, it would be important to have a tool that can reliably segment, not just the brain, but the entire head in the presence of lesions and abnormal anatomy.

Currently, automatic segmenters such as SPM[15], FSL[16], and DeepMedic[17], all perform well on individuals with normal anatomy. There are also tools, which perform detailed segmentation of different areas within the brain, such as hippocampus, midbrain, cerebellum[18] or even detailed perceptions of cortical tissue[19]. Unfortunately, these tools struggle with abnormal anatomy or lesions. A number of tools have been developed to identify tumors[20] or lesions related to MS[21] and ALS[22]. There are also some existing methods to delineate chronic stroke lesions such as LINDA[23]. However, to our knowledge, these methods do not carefully segment non-brain tissues, even in normal anatomies, beyond “skull stripping”. In the context of current flow modeling, skull, CSF and non-brain soft tissue are equally important given their drastic difference in electric conductivity[24] (skull: 0.02 S/m, CSF: 1.71 S/m, scalp: 0.41 S/m). Current flow models are important to compute “lead fields” that are used in current source reconstructions in MEG/EEG, or to target specific brain areas with TES/TMS. Segmentation tools developed in these contexts, such as in ROAST[11], [12], BrainStorm[13], and SimNIBS[14], work well on normal anatomy, but again, fail in the presence of lesions. Therefore, there is a need for an automatic MRI brain segmentation tool that will perform reliably in cases with abnormal anatomy.

Traditional methods, such as SPM and FSL rely on relatively simple intensity features and a tissue probability map (TPM). We

improved on this approach by extracting more complex features using a convolutional network and adding morphological priors. When trained on lesioned anatomies, this “MultiPriors” network[25] improved performance compared to SPM and FSL. Unfortunately, aligning the TPM to the MRI has remained a persistent challenge in the presence of abnormal anatomy.

Here we developed a new deep network without the need to align on an atlas. Instead, the network was trained on a larger corpus of clinical scans with chronic stroke or disorder of consciousness (typically resulting from traumatic brain injury). The network is based on a standard 2D U-Net[26] that efficiently and reliably segments MRIs into 7 tissue classes. In this work we focus on the task of segmenting the whole head in subjects with abnormal brain anatomy, which remains a challenging problem. An important part of this new work was to generate the corresponding manually annotated dataset for training and testing. We compared performance to our MultiPrior model and newer deep networks, such as Brainchop[27] (developed for light-weight processing in a web browser) and Synthseg[28] (developed to operate on multiple modalities). The results we report here set a new state-of-the-art for automatic segmentation of the whole head for both normal and abnormal anatomies. We release the network and data that was used for testing in the hope that it can serve as a benchmark for future efforts.

II. METHODS

A. Head MRI from patients with chronic abnormalities and healthy subjects

The data was collected from four different institutions from patients with different clinical conditions (See Table 1). All scans are T1-weighted MRI from a total of 93 individuals as follows: 4 scans from healthy subjects (Gender: 4M/ 0F, Ethnicity: 1 Asian, 3 White (not Latino), Age: 30-50) obtained on a 3T Siemens Trio scanner (Erlangen, Germany)[29]; 50 patients with chronic aphasia stroke collected at Georgetown University (Gender: 18M/ 10F, Ethnicity: 1 Asian, 8 Black, 17 White (not Latino), 1 White/Latino, 1 Unknown, Age: 41-75) imaged on a Siemens Trio 3T scanner and University of North Carolina, Chapel Hill (Gender: 16M/ 5F/ 1 Unknown, Ethnicity: 8 Black, 14 White (not Latino), Age: 44-75), imaged on a 3T Siemens Biograph mMR scanner; 32 subjects with disorders of consciousness collected at the Pitie-Salpetriere University Hospital in Paris, imaged on a 3T General Electric Signa system Milwaukee, WI (Demographics not disclosed) and 7 patients with chronic aphasia and apraxia of speech subsequent to stroke collected at New York University (Gender: 6 M/1 W, Ethnicity: 6 White (not Latino), 1 White/Latino, Age: 54-83), imaged on a 3T Siemens Prisma scanner. Patients had the lesion or injuries occur at least 6 months prior to the MRI scan, at which point the lesioned brain area is largely replaced by CSF. All scans have isotropic resolution of 1mm. All data was collected with IRB approval. Public release of the de-identified dataset is available on Kaggle[30] as version 1.

B. Creation of segmentation labels

For all available MRIs we generated volumetric segmentations labeling all voxels into one of seven possible categories: Background (extracerebral air), air cavities, white

matter (WM), gray matter (GM), cerebrospinal fluid (CSF), bone and non-brain soft tissue. These labels were obtained for the full 3D volume using semi-manual segmentation. Specifically, healthy (N=3) and aphasia stroke heads (N=50) were first segmented automatically using SPM (version 8), touched up by an in-house Matlab script[29], and then manually corrected using scanIP (Synopsys, Mountain View, CA). Manual correction focused on the stroke lesions and boundaries between CSF, gray matter and skull boundary. One head from a previous study[31] had been fully segmented manually using ScanIP.

For the stroke patients with apraxia (N=7) and patients with Disorders of Consciousness (N=32), the head MRIs were segmented using Multipriors[25] through ROAST[12] which utilized SPM12 for coregistration with a TPM. Post-processing steps in Python addressed common segmentation errors, such as mislabeled background within the skull and sinus, bone touching brain matter instead of CSF, skin mislabeled as CSF, and air mislabeled as bone. A custom Python script corrected these errors by relabeling bone in contact with the brain as CSF, converting background within skin regions to bone, and reclassifying sinus cavities outside the head as background. Despite these automated corrections, manual relabeling was essential to address residual errors, ensuring accurate and anatomically reliable segmentations. Manual adjustments using MRICron’s[32] drawing tools corrected significant anatomical mistakes, particularly in regions where skin, CSF, and air were mislabeled.

Table 1: Overview of the data used for training and testing and public release.

Data set	MRI	Labels	Train	Test	Data release
Normal	4	1 manual +3 SPM + manual correction	4	3 (cross validated)	Original MRI + training labels
Chronic Aphasia Stroke	43	SPM + manual correction	43	43 (cross validated)	Refaced MRI + training labels
Chronic Aphasia Stroke	7	SPM + manual correction	0	7	Refaced MRI + training labels
Chronic Apraxia Stroke	7	MultiPrior + manual correction	7	0	Refaced MRI
Disorders of Consciousness	32	MultiPrior + manual correction	32	0	None

C. Anonymization for public data release

For anonymization purposes, the reface tool of AFNI[33], [34] was used, which provides three methods of face removal or replacement: deface, reface, and reface+. The reface option adds an average face to the MRI, while reface+ also generates a uniform head shape. However, reface+ generates unrealistic scalp/skull anatomy and will not be considered here.

D. Data preprocessing

Harmonization of the input involved resampling the MRI to 1 mm isotropic resolution if needed, reoriented to ‘RAS’ (right - anterior - superior), and resizing to 256x256x256 voxels through padding/cropping. Intensity normalization was done by dividing by each image’s 95 percentile.

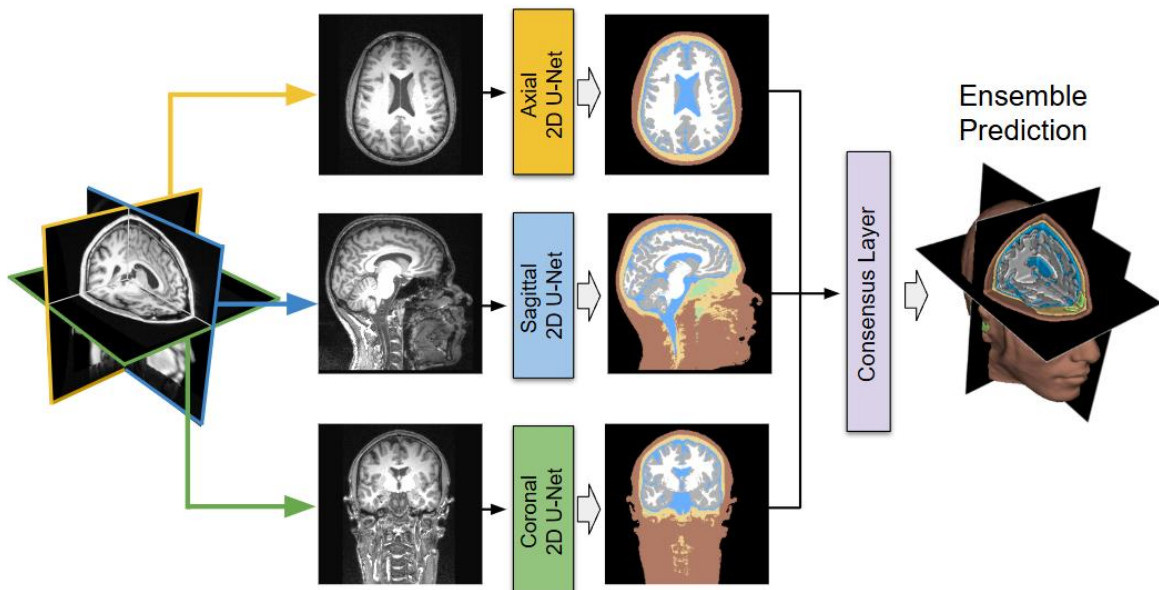


Figure 1: Overview of the MultiAxial model for segmentation of head MRI. An input T1 weighted MRI is processed in each axis (axial, sagittal and coronal) by a separate 2D U-Net, each of which output probabilities per pixel for belonging to one of seven classes: Background (black), Air/Sinus cavities (light green), White Matter (white), Gray Matter (gray), Cerebrospinal fluid (CSF, light blue), bone (light yellow) and skin (brown). The probabilities from each model are merged into a single volume by the consensus layer, consisting of a single convolutional layer.

E. Model architecture and training

We utilized three 2D U-Nets to process 2D slices of the MRI in each of the three orthogonal axes: Sagittal, Coronal and Axial. The three models have identical architecture but their own set of weights. Each model outputs the probability of belonging to one of 7 possible tissue classes for each pixel in the volume. We use a single convolutional layer to merge these three probabilities into a single output, referred to as a “consensus layer” (Figure 1).

The input dimension is fixed to 256x256 for all models, processed by 6 convolutional blocks each consisting of 2 convolutional layers with kernel size (3,3) and ReLU activation[35], followed by a downsampling layer with a pool size of (2,2). The upsampling is done by 6 convolutional blocks with a transposed convolutional layer instead. Each of the three models has a total of approximately 1 million trainable parameters. The network also takes as input the coordinates of the image to provide for spatial awareness as a matrix with three channels, encoding each of the x,y,z axes. This spatial information is concatenated before the last two layers of the network. During training, the network uses the Adam optimizer[36] with a learning rate of 1e-5 and a dice loss function for multiclass classification.[37], [38]

F. Model selection and training

A total of 93 heads were used for training and testing, with 53 used for testing (7 exclusively used for testing and 46 overlapping between train and test using cross-validation; see Table 1). Each cross-validation run split 86 heads into training+validation+testing (four runs split as 65+12+9 and one run as 64+12+10). Slices that contain only background from the boundaries of each MRI were removed from the training data. Selection of model and training hyperparameters was done using the validation set for performance evaluation.

G. Evaluation and benchmarks

We compare model performance on the test set using the following pre-trained and released models: Multipriors, BrainChop and SynthSeg. For the evaluation metric we use the Dice score, which measures overlap between masks ranging from 0 (no overlap) to 1 (perfect overlap). We average Dice scores across tissues and report the median Dice score across subjects.

We used the Multipriors model as implemented in the software ‘ROAST’. This convolutional neural network takes as an input a Tissue Probability Map (TPM), which needs to be aligned with the input MRI. Within this software, the TPM alignment is performed by SPM12. However due to alignment errors we also use the previous version, SPM8, which is more robust for this step with default parameters.

BrainChop was implemented following instructions provided on the BrainChop GitHub[39] repository. BrainChop was installed with Pip and ran with the terminal command: "brainchop -i <input> -o <output> -m -subcortical." Following recommendations by BrainChop developers, we used the robust subcortical-plus-gray-white-matter model, which outputs a segmentation with 14 classes within the brain, corresponding to parcellation of different brain regions. To obtain a segmentation of only white and gray matter instead, we mapped these 14 regions to two classes by overlapping the BrainChop output with our ground-truth labels, determining which regions correspond to either white or gray matter. Small isolated connected components were removed using the connected-components-3d library.

SynthSeg was implemented following instructions provided on the SynthSeg Github[40] repository. We cloned the repository, created a virtual environment with the required dependencies, downloaded the model files, and ran the following terminal command: "python ./scripts/commands/SynthSeg_predict.py --i <input> --o <output> --robust." We used the robust model, which outputs a segmentation with 44 classes within the brain. The same mapping process as used for BrainChop was applied to classify the

output into gray matter and white matter. For both BrainChop and SynSeg Dice scores were calculated only for gray matter and white matter.

We also evaluate the effect of different segmentation results on current flow models using the software ROAST. For this we calculated the lead field on one of the aphasia stroke cases using the 'leadField' option to the roast command. We calculated lead fields for segmentations using five different methods: SPM12, Multipriors with SPM12, Multipriors with SPM8, Multiaxial, and Manual Ground Truth Labels. Next, we selected an optimal electrode montage to target a particular brain area using `roast_target[41], [42], [43]` command. As a target we picked a location near the lesion that corresponds to gray matter in all segmentations.

III. RESULTS

We utilized the validation set performance to select hyperparameters and model architecture (Fig. 2). Based on this, we train a model with a depth of 6 layers (1,016,839 trainable parameters, Fig 2C) and data augmentation consisting of random rotations and shearings at 15 degrees and addition of spatial information as an extra input (Fig. 2A). We add an extra input with voxel coordinates such that each model has global spatial information (Fig. 2B). We also compare two ways of merging the outputs of the models operating in each axis (sagittal, coronal and axial) by implementing a majority vote method as well as a convolutional layer (Fig. 2D). For development and training of this layer see supplement (Fig. S1).

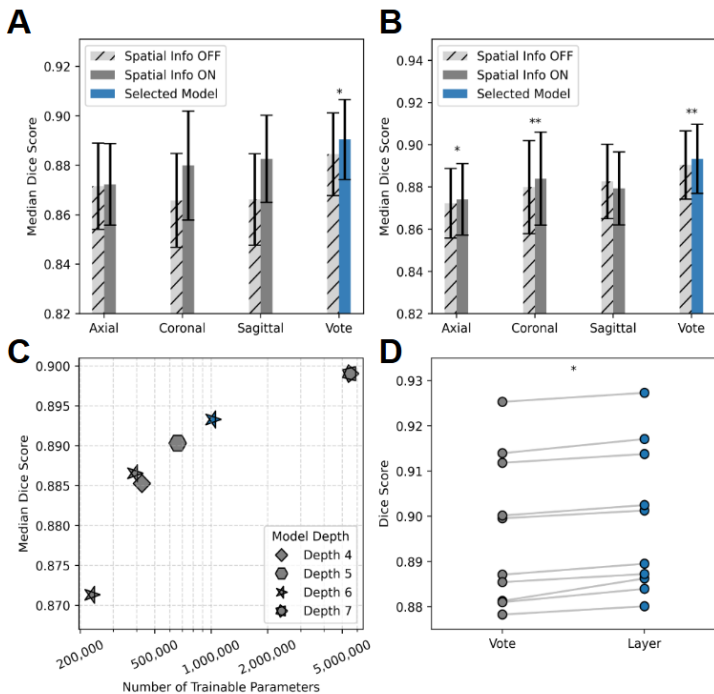


Figure 2: Model selection on a validation set. A: Determines the benefit on Dice score of including data augmentation. B: Determines the benefit on Dice score of including voxel coordinates as additional input. C: Determines the benefit of increasing depth and width of the U-Net, which implies increase in the number of parameters. D: Determines the benefit of using a CNN consensus layer compared with a median vote consensus for merging the output of the three models operating in each orthogonal direction.

A. Performance against other available AI-tools for segmentation of brain MRI

We compare the performance on the test set against our previously developed model 'MultiPriors' that depends on SPM for alignment of a TPM, as well as SPM12's segmentation tool. Dice scores were highest for the MultiAxial model as well as for the published MultiPriors

model using SPM8 (Fig. 3A). Median Dice scores \pm IQR for each segmentation type: Multiaxial 0.879 ± 0.041 , Multipriors (SPM8) 0.880 ± 0.0389 , Multipriors (SPM12) 0.850 ± 0.0786 , SPM12 0.798 ± 0.0992 , Friedman test Chi-square: $F=1.21e+02$, $p\text{-value}=4.09e-26$, Wilcoxon Test with Bonferroni correction: Multiaxial vs Multipriors (SPM8) $W=6.93e+02$ $p\text{-value}=8.42e-01$, Multipriors (SPM8) vs Multipriors (SPM12) $W=1.20e+01$ $p\text{-value}=4.73e-10$, Multipriors (SPM12) vs SPM12 $W=6.50e+01$ $p\text{-value}=8.48e-09$, $N=53$. Bonferroni correction threshold for significance $p\text{-value} < 0.00833$.

Noticeably, SPM12 struggles more often in the TPM alignment step, influencing the resulting segmentation (Fig. 3C). Dice scores for brain tissue were compared against two publicly available AI-tools SynthSeg and BrainChop, as these models only provide labels for brain structures. MultiAxial outperformed both models in the test set (Fig. 3B&D)

Median Brain Dice scores \pm IQR for each segmentation type: Multiaxial 0.898 ± 0.0412 , SynthSeg 0.817 ± 0.0536 , BrainChop 0.757 ± 0.125 , Friedman test Chi-square: $F=1.06e+02$, $p\text{-value}=9.60e-24$, Wilcoxon Test with Bonferroni correction: Multiaxial vs SynthSeg: $W=0.0$ $p\text{-value}=2.39e-10$, Synthseg vs BrainChop: $W=0.0$ $p\text{-value}=2.39e-10$, $N=53$. Bonferroni correction threshold for significance $p\text{-value} < 0.0167$

B. Anonymization of head MRI and model performance in defaced data

The MultiAxial model achieved similar Dice scores for defaced and refaced MRI images (Fig. 4). This was evaluated on structures inside the skull, which should remain unaltered by defacing, including gray matter and white matter. Median Dice scores \pm IQR for each MRI type: Original MRI 0.898 ± 0.0412 , Defaced MRI 0.887 ± 0.052 , Refaced MRI 0.893 ± 0.0515 . Friedman test Chi-square: $F=5.05e+01$, $p\text{-value}=1.07e-1$. Wilcoxon Test: Original vs Deface $W=6.10e+01$, $p\text{-value}=6.87e-09$, Deface vs Reface $W=5.12e+02$, $p\text{-value}=7.16e-02$, $N=53$. Bonferroni correction threshold for significance $p\text{-value} < 0.0167$. This demonstrates that, even when using anonymized MRIs such as defaced and refaced data, the model maintains strong performance with comparable Dice scores despite significant differences between groups

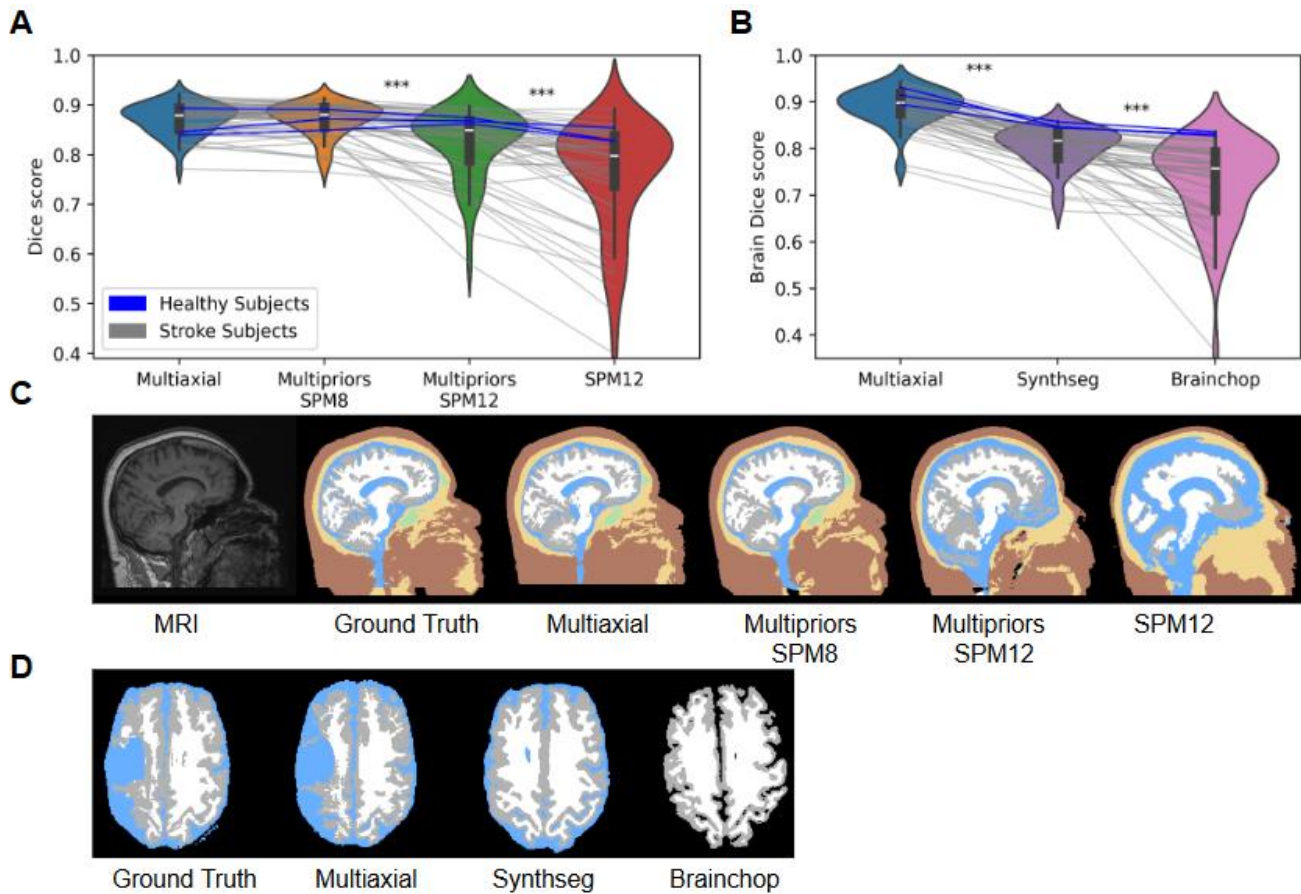


Figure 3: Performance comparison between segmentation tools. **A:** Test set Dice scores for head MRI segmentation with Multiaxial and Multipriors. The alignment of the atlas required by Multipriors was done with ROAST, which relies on SPM8 or SPM12 depending on version number. **B:** Test set Dice scores for segmentation of brain (white matter and gray matter) using Multiaxial, Synthseg and Brainchop. **C:** Example segmentation (sagittal view) for models compared in panel A, in the same order. **D:** Example brain segmentation (axial view) for models compared in panel B, in the same order. The ground-truth shows a CSF-filled stroke lesion in the left hemisphere that is missed by SynthSeg and BrainChop

C. Improvement of a current flow modelling software

To test the effect of segmentations on current flow models we used the ROAST software (Fig. 5A). In order to inspect the sensitivity of the resulting field magnitude, we ran five current flow simulations on the same head, but with segmentations from different models. We used the same electrode placement across all segmentations, and obtained similar field magnitudes for the Ground Truth, Multiaxial and Multipriors (with TPM alignment by SPM8) segmentations. However, results differed substantially for the SPM12 segmentation, or Multipriors (with TPM alignment by SPM12) (Fig. 5B).

An advantage of MultiAxial is processing speed. As the model operates in 2D it requires less memory and gains in speed compared to previous methods (see Table 2), with exception of BrainChop that has been optimized for GPU usage.

Table 2: Processing speeds in minutes:seconds evaluated on the same MRI either using a GPU (NVIDIA RTX A5000, 24 GB RAM) or a CPU (Intel Core i7-8700K, 64 GB RAM) on Windows 11.

Model	MultiAxial	MultiPrior*	SPM8	SPM12	BrainChop	SynthSeg
CPU time	1:19	2:23	9:49	7:09	17:29	7:46
GPU time	0:20	1:18	NA	NA	0:08	1:28

* Includes warping for spatial alignment of a TPM, but assumes that the warping field has been pre-computed with SPM.

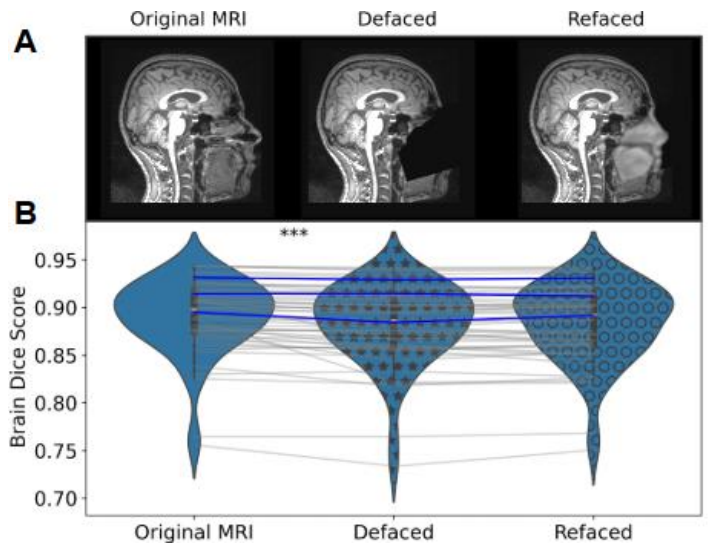


Figure 4: Robust segmentation of the brain on de-identified head MRI. **A:** Example of two de-identification methods in ANFI applied to a healthy subject: 'Deface' removes identifiable features by removing the face from the image. 'Reface' replaces the face with an average of multiple aligned faces. **B:** Dice scores for segmentation of brain tissue (white matter and gray matter) on the original MRI, defaced MRI and 'Refaced' MRI.

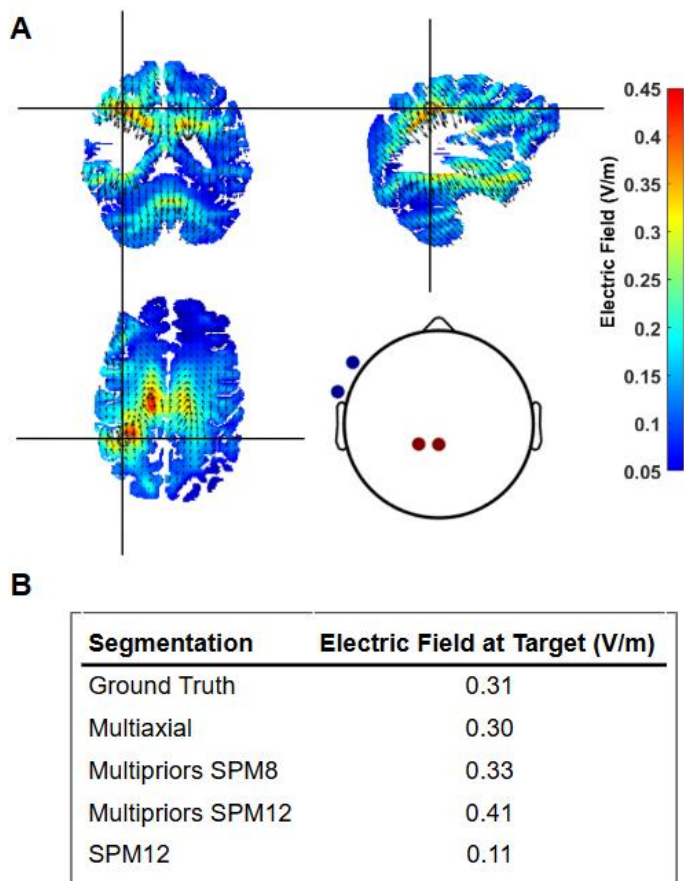


Figure 5: Current flow modelling in the brain given a target. An MRI from a subject with a large stroke lesion was used for current flow modeling using the software ‘ROAST’. A: Simulated electric field in the brain for a particular electrode montage (bottom right). This montage was optimized to generate maximum field magnitude at the target location (cross hair) under maximum 1mA current in each electrode. This simulation used the Ground Truth segmentation. B: Comparison of the electric field magnitude at the specified target when using different methods for segmentation.

IV . DISCUSSION

The most wide-spread tools for brain signal analysis require a detailed segmentation of the brain, and to do so, they rely on an atlas for segmentation, such as a TPM in SPM, or in FAST as part of FSL[44], or a multi-atlas segmentation in ANTs[45]. These methods are susceptible to misalignment when registering an atlas of normal anatomy to an individual MRI with abnormal anatomy. Additionally, these atlases assume normal anatomy and thus introduce incorrect biases in the segmentation. The new MultiAxial model eliminates the dependency on an atlas, thereby simplifying the processing and gaining in robustness. We overcame this dependency by training the AI on a large number of heads with abnormal anatomy (N=65 for training plus N=12 for model selection). The resulting model shows state-of-the-art performance, not only of clinical scans, but also on normal anatomy. Crucially, we are publicly releasing the training data and model to serve as a benchmark and basis for future development efforts.

The dataset compiled and released here is unique in that we included cases with chronic stroke and traumatic brain injury. These cases are characterized by extended ventricles and fluid-filled voids where one would usually expect brain tissue. In

contrast, existing clinical datasets are mostly focused on brain tumors, such as the International Brain Tumor Segmentation (BraTS) Challenge,⁴¹ which provides labels only for the tumors. The 2012 dataset contained 65 high and low grade gliomas[46]. The 2015 dataset contains 220 high grade and 54 low grade gliomas for training and 94 unpublished cases reserved for blinded testing[47]. This dataset was recently extended in the BraTS 2024 release with approximately 4,500 cases.[48], [49] DeepMedic[17], released in 2016, was one of the first AI models trained on the BraTS data. We added to the DeepMedic architecture prior probabilities to generate the MultiPrior model and trained it on whole head segmentation of normal and stroke anatomies.[25]

Our focus in compiling new data was unique in that we generated labels and evaluated performance on the entire head, not just the brain. There is in general a shortage of high-quality manual annotated MRI datasets.[50], [51] Comprehensive manual corrections and whole-head manual tissue annotations in 3D are particularly time-consuming and rely on trained personnel. The majority of brain MRI datasets are skull-stripped (BraTS[48], MICA[52],HCP[53], Mindboggle[54], ADNI[55]), omitting key anatomical features outside the brain, which restricts their utility for tasks requiring full-head analysis, such as modeling of current flow in brain stimulation studies. As a result, datasets that have been manually segmented are often small in size, (N=39 Synthseg[28], N=5 Brainchop[27]).

Newer AI models, such as Brainchop and Synthseg are trained on large datasets segmented with FreeSurfer[56] to generate gray and white matter labels. Brainchop,[27] which employs Catalyst.Neuro’s[57], [58], [59] model, used 1200 healthy heads from Human Connectome Project (HCP)[53], [60] and 101 heads from Mindboggle.[54], [61] Synthseg[62] used a mix of data totaling 686 heads in a mix of healthy subjects and patients with memory complaints and Alzheimer’s from Alzheimer’s Disease Neuroimaging Initiative (ADNI)[55], [63]. The focus of these models is parcellation of the brain, and assume that the overall brain anatomy is well captured with traditional segmentation methods. However, as we have seen, these models struggle with abnormalities that erroneously classify stroke damage as gray or white matter when the area is now filled with CSF. The present model, to our knowledge, is the only model to have been trained on chronic stroke and disorder of consciousness patients, that are characterized by large CSF-filled voids.

Many older segmentation tools suffer from outdated codebases, poor documentation, and reliance on deprecated Python libraries. In contrast, our model is fully integrated into ROAST, offering ease of use. Its batch script automatically sets up the environment, enabling segmentation without requiring command-line expertise. Furthermore, our model is lightweight, self-contained and boasts minimal dependencies, ensuring seamless compatibility across Windows, macOS, and Linux—a clear advantage over older tools that often exclude Windows compatibility such as Synthseg[28], AFNI²⁸[45], FreeSurfer[56], FSL[16], Deepmedic[17] which require implementing a Linux or macOS environment. Such requirements can present a considerable barrier for new users, making our solution a more accessible and user-friendly alternative.

The MultiAxial model has a field of view (FOV) equal to a complete side-view of the MRI in each direction (sagittal, axial and coronal), meaning that the prediction output for any given pixel is influenced by the input features from locations far away. This is in contrast to common implementations of 3D networks (such as the DeepMedic or MultiPriors) which, in order to satisfy VRAM limitations, make predictions based on small cubes at a time. A larger FOV provides spatial awareness which reduces mistakes, which is why methods such as SPM and MultiPriors rely on tissue probability maps for a proper result. On the other hand we observed that distant regions influence the model outputs: Defaced inputs have slightly different segmentation results on the brain, despite the defacing process not affecting the brain areas.

Our model employs a consensus layer rather than traditional ensemble methods like voting or averaging. Voting combines 2D segmentations by selecting the pixel class with mutual agreement. In cases of disagreement, it defaults to the most common or highest-confidence class. Averaging is typically used for binary classifications like lesions vs. non-lesions but is unsuitable for our multi-class segmentation due to non-numerically separable class values. Our consensus layer integrates segmentations from all three 2D views and the MRI data to achieve superior segmentation accuracy.

In this work, the Dice score for the brain is usually around 90% and a few points less when including the entire head. What is the source of the remaining 10% errors? We have shown evidence that some of these errors may be due to inaccurate “truth data”. As in previous work, the target labels were largely generated automatically, with some relatively minor corrections (in terms of overall volume altered by manual correction). We believe that the network indeed may produce more accurate segmentations than the manual labels. This is consistent with the somewhat higher performance for the brain, as manual correction was generally more careful for the brain and CSF in this data, and less effort went into fixing the non-brain soft tissue covering skin, scalp and other soft tissues, which all received a single label. On the flip side, we acknowledge an upwards bias in the results, because SPM and MultiPrior were used to produce the first round of “truth” labels, and the network was trained on those. The MultiAxial network was trained to reproduce the result of those algorithms and may thus have an upwards bias in performance. In summary, the 10% residual “error” in performance may be an optimistic estimate due to the bias of semi automatic truth labels, or it may be an underestimate due to insufficient manual corrections in the truth data. Regardless of this, a Dice score of 0.9 represents a significant milestone, outperforming most prior benchmarks. On normal anatomy we achieve a median performance of 0.915, which is comparable to FreeSurfer[64] which reports Dice scores around 0.91[57] on GWM brain segmentation. For more detailed parcellation within the brain, FreeSurfer reports between 0.85 and 0.88. SynthSeg[28] reports a median of 0.88, SAMSEG[65] a score of 0.85, while generalized models like T1 Baseline[66] and nnUNet,[67] specifically trained on T1-weighted images, both achieve scores of 0.91. For brain tumor segmentation, nnUNet[68] achieves Dice scores of 0.884, 0.888, and 0.932 for enhancing tumor, tumor core, and whole tumor, respectively. Similarly, Swin UNETR[69] reports scores of 0.853, 0.876, and 0.927 for these categories. In total, the current model, MultiAxial, sets a new state-of-the-art for non-brain tissue of the head, is on par with

segmentation of brain tissue, and significantly outperformed existing models on abnormal anatomy.

To support further research, we are releasing a manually labeled stroke MRI dataset unavailable elsewhere. This dataset includes annotations for seven tissue classes, offering invaluable resources for advancements in stroke research and related applications.

V. CONCLUSION

We make a public open-source release of a state-of-art model leveraging spatial information and volumetric information for segmentation of tissues in head MRI robust to clinical abnormalities, as well as a public release of a labeled data-set of clinical MRI. We implement the developed model as part of a pre-existing pipeline for current flow simulation in ROAST, making it robust for handling abnormal clinical MRI where previous software failed. Models and first version of the data available on Github[70] and Kaggle[30].

VI. ACKNOWLEDGMENT

We would like to thank Jacobo D. Sitt at Pitie-Salpetriere University Hospital in Paris for the help in gathering and sharing the dataset on disorders of consciousness (not released).

REFERENCES

- [1] Stephen J. Gardner MS, Joshua Kim PhD, and Indrin J. Chetty PhD, “Modern Radiation Therapy Planning and Delivery.” Accessed: Dec. 06, 2024. [Online]. Available: <https://www.clinicalkey.com/#!/content/playContent/1-s2.0-S088985881930098X?returnurl=null&referrer=null>
- [2] H. Hyare, S. Thust, and J. Rees, “Advanced MRI Techniques in the Monitoring of Treatment of Gliomas,” *Curr. Treat. Options Neurol.*, vol. 19, no. 3, p. 11, Mar. 2017, doi: 10.1007/s11940-017-0445-6.
- [3] H. Alloui, M. Sadgal, and A. Elfazziki, “Deep MRI Segmentation: A Convolutional Method Applied to Alzheimer Disease Detection,” *Int. J. Adv. Comput. Sci. Appl.*, vol. 10, no. 11, 2019, doi: 10.14569/IJACSA.2019.0101151.
- [4] C. Ledig *et al.*, “Robust whole-brain segmentation: Application to traumatic brain injury,” *Med. Image Anal.*, vol. 21, no. 1, pp. 40–58, Apr. 2015, doi: 10.1016/j.media.2014.12.003.
- [5] X. Ren, J. Huo, K. Xuan, D. Wei, L. Zhang, and Q. Wang, “Robust Brain Magnetic Resonance Image Segmentation for Hydrocephalus Patients: Hard and Soft Attention,” in *2020 IEEE 17th International Symposium on Biomedical Imaging (ISBI)*, Apr. 2020, pp. 385–389. doi: 10.1109/ISBI45749.2020.9098541.
- [6] A. Clèrigues, S. Valverde, J. Bernal, J. Freixenet, A. Oliver, and X. Lladó, “Acute and sub-acute stroke lesion segmentation from multimodal MRI,” *Comput. Methods Programs Biomed.*, vol. 194, p. 105521, Oct. 2020, doi: 10.1016/j.cmpb.2020.105521.
- [7] J. A. Stokum, V. Gerzanich, and J. M. Simard, “Molecular pathophysiology of cerebral edema,” *J. Cereb. Blood Flow Metab.*, vol. 36, no. 3, pp. 513–538, Mar. 2016, doi: 10.1177/0271678X15617172.
- [8] Juhasz C *et al.*, “White matter volume as a major predictor of cognitive function in Sturge-Weber syndrome,” *Arch. Neurol.*, vol. 64, no. 8, pp. 1169–1174, Aug. 2007, doi: 10.1001/archneur.64.8.1169.
- [9] J. A. Meltzer, M. Negishi, L. C. Mayes, and R. T. Constable, “Individual differences in EEG theta and alpha dynamics during working memory correlate with fMRI responses across subjects,” *Clin. Neurophysiol. Off. J. Int. Fed. Clin. Neurophysiol.*, vol. 118, no. 11, pp. 2419–2436, Nov. 2007, doi: 10.1016/j.clinph.2007.07.023.
- [10] A. Datta, “Inter-Individual Variation during Transcranial Direct Current Stimulation and Normalization of Dose Using MRI-Derived

- Computational Models,” *Front. Psychiatry*, vol. 3, Oct. 2012, doi: 10.3389/fpsy.2012.00091.
- [11] Y. Huang, A. Datta, M. Bikson, and L. C. Parra, “ROAST: An Open-Source, Fully-Automated, Realistic Volumetric-Approach-Based Simulator For TES,” in *2018 40th Annual International Conference of the IEEE Engineering in Medicine and Biology Society (EMBC)*, Jul. 2018, pp. 3072–3075. doi: 10.1109/EMBC.2018.8513086.
- [12] Y. Huang, A. Datta, M. Bikson, and L. C. Parra, “Realistic volumetric-approach to simulate transcranial electric stimulation-ROAST—a fully automated open-source pipeline,” *J. Neural Eng.*, vol. 16, no. 5, p. 056006, Jul. 2019, doi: 10.1088/1741-2552/ab208d.
- [13] F. Tadel, S. Baillet, J. C. Mosher, D. Pantazis, and R. M. Leahy, “Brainstorm: A User-Friendly Application for MEG/EEG Analysis,” *Comput. Intell. Neurosci.*, vol. 2011, p. 879716, 2011, doi: 10.1155/2011/879716.
- [14] A. Thielscher, A. Antunes, and G. B. Saturnino, “Field modeling for transcranial magnetic stimulation: A useful tool to understand the physiological effects of TMS?,” in *2015 37th Annual International Conference of the IEEE Engineering in Medicine and Biology Society (EMBC)*, Aug. 2015, pp. 222–225. doi: 10.1109/EMBC.2015.7318340.
- [15] J. Ashburner and K. J. Friston, “Unified segmentation,” *NeuroImage*, vol. 26, no. 3, pp. 839–851, Jul. 2005, doi: 10.1016/j.neuroimage.2005.02.018.
- [16] S. M. Smith *et al.*, “Advances in functional and structural MR image analysis and implementation as FSL,” *NeuroImage*, vol. 23 Suppl 1, pp. S208–219, 2004, doi: 10.1016/j.neuroimage.2004.07.051.
- [17] K. Kamnitsas *et al.*, “DeepMedic for Brain Tumor Segmentation,” A. Crimi, B. Menze, O. Maier, M. Reyes, S. Winzeck, and H. Handels, Eds., in *Lecture Notes in Computer Science*, vol. 10154. Cham: Springer International Publishing, 2016, pp. 138–149. doi: 10.1007/978-3-319-55524-9_14.
- [18] S. Nigro *et al.*, “Fully Automated Segmentation of the Pons and Midbrain Using Human T1 MR Brain Images,” *PLOS ONE*, vol. 9, no. 1, p. e85618, Jan. 2014, doi: 10.1371/journal.pone.0085618.
- [19] K. Kushibar *et al.*, “Automated sub-cortical brain structure segmentation combining spatial and deep convolutional features,” *Med. Image Anal.*, vol. 48, pp. 177–186, Aug. 2018, doi: 10.1016/j.media.2018.06.006.
- [20] S. Pereira, A. Pinto, V. Alves, and C. A. Silva, “Brain Tumor Segmentation Using Convolutional Neural Networks in MRI Images,” *IEEE Trans. Med. Imaging*, vol. 35, no. 5, pp. 1240–1251, May 2016, doi: 10.1109/TMI.2016.2538465.
- [21] C. Gros *et al.*, “Automatic segmentation of the spinal cord and intramedullary multiple sclerosis lesions with convolutional neural networks,” *NeuroImage*, vol. 184, pp. 901–915, Jan. 2019, doi: 10.1016/j.neuroimage.2018.09.081.
- [22] H. K. van der Burgh, R. Schmidt, H.-J. Westeneng, M. A. de Reus, L. H. van den Berg, and M. P. van den Heuvel, “Deep learning predictions of survival based on MRI in amyotrophic lateral sclerosis,” *NeuroImage Clin.*, vol. 13, pp. 361–369, Jan. 2017, doi: 10.1016/j.nicl.2016.10.008.
- [23] D. Pustina, H. B. Coslett, P. E. Turkeltaub, N. Tustison, M. F. Schwartz, and B. Avants, “Automated segmentation of chronic stroke lesions using LINDA: Lesion identification with neighborhood data analysis,” *Hum. Brain Mapp.*, vol. 37, no. 4, pp. 1405–1421, 2016, doi: 10.1002/hbm.23110.
- [24] H. McCann, G. Pisano, and L. Beltrachini, “Variation in Reported Human Head Tissue Electrical Conductivity Values,” *Brain Topogr.*, vol. 32, no. 5, pp. 825–858, 2019, doi: 10.1007/s10548-019-00710-2.
- [25] L. Hirsch, Y. Huang, and L. C. Parra, “Segmentation of MRI head anatomy using deep volumetric networks and multiple spatial priors,” *J. Med. Imaging Bellingham Wash*, vol. 8, no. 3, p. 034001, May 2021, doi: 10.1117/1.JMI.8.3.034001.
- [26] O. Ronneberger, P. Fischer, and T. Brox, “U-Net: Convolutional Networks for Biomedical Image Segmentation,” May 18, 2015, *arXiv*: arXiv:1505.04597. doi: 10.48550/arXiv.1505.04597.
- [27] M. Masoud, F. Hu, and S. Plis, “Brainchop: In-browser MRI volumetric segmentation and rendering,” *J. Open Source Softw.*, vol. 8, no. 83, p. 5098, Mar. 2023, doi: 10.21105/joss.05098.
- [28] B. Billot *et al.*, “SynthSeg: Segmentation of brain MRI scans of any contrast and resolution without retraining,” *Med. Image Anal.*, vol. 86, p. 102789, May 2023, doi: 10.1016/j.media.2023.102789.
- [29] Y. Huang, J. P. Dmochowski, Y. Su, A. Datta, C. Rorden, and L. C. Parra, “Automated MRI Segmentation for Individualized Modeling of Current Flow in the Human Head,” *J. Neural Eng.*, vol. 10, no. 6, p. 10.1088/1741-2560/10/6/066004, Dec. 2013, doi: 10.1088/1741-2560/10/6/066004.
- [30] “Full-Head MRI & Segmentation with Abnormal Anatomy.” Accessed: Jan. 29, 2025. [Online]. Available: <https://www.kaggle.com/datasets/andrewbirnbaum/full-head-mri-and-segmentation-with-abnormal-anatomy>
- [31] A. Datta, V. Bansal, J. Diaz, J. Patel, D. Reato, and M. Bikson, “Gyri-precise head model of transcranial direct current stimulation: Improved spatial focality using a ring electrode versus conventional rectangular pad,” *Brain Stimulat.*, vol. 2, no. 4, pp. 201–207.e1, Oct. 2009, doi: 10.1016/j.brs.2009.03.005.
- [32] C. Rorden and M. Brett, “Stereotaxic display of brain lesions,” *Behav. Neurol.*, vol. 12, no. 4, pp. 191–200, 2000, doi: 10.1155/2000/421719.
- [33] R. Cox and P. Taylor, “Why de-face when you can re-face?,” 26th Annual Meeting of the Organization for Human Brain Mapping, 2020. [Online]. Available: https://afni.nimh.nih.gov/pub/dist/HBM2020/AFNI_reface_OHBM2020.pdf
- [34] A. E. Theyers *et al.*, “Multisite Comparison of MRI Defacing Software Across Multiple Cohorts,” *Front. Psychiatry*, vol. 12, Feb. 2021, doi: 10.3389/fpsy.2021.617997.
- [35] A. F. Agarap, “Deep Learning using Rectified Linear Units (ReLU),” Feb. 07, 2019, *arXiv*: arXiv:1803.08375. doi: 10.48550/arXiv.1803.08375.
- [36] D. P. Kingma and J. Ba, “Adam: A Method for Stochastic Optimization,” Jan. 30, 2017, *arXiv*: arXiv:1412.6980. doi: 10.48550/arXiv.1412.6980.
- [37] W. R. Crum, O. Camara, and D. L. G. Hill, “Generalized overlap measures for evaluation and validation in medical image analysis,” *IEEE Trans. Med. Imaging*, vol. 25, no. 11, pp. 1451–1461, Nov. 2006, doi: 10.1109/TMI.2006.880587.
- [38] C. H. Sudre, W. Li, T. Vercauteren, S. Ourselin, and M. J. Cardoso, “Generalised Dice overlap as a deep learning loss function for highly unbalanced segmentations,” vol. 10553, 2017, pp. 240–248. doi: 10.1007/978-3-319-67558-9_28.
- [39] *neuroneural/brainchop*. (Dec. 11, 2024). JavaScript. *neuroneural*. Accessed: Dec. 11, 2024. [Online]. Available: <https://github.com/neuroneural/brainchop>
- [40] BBillot, *BBillot/SynthSeg*. (Dec. 10, 2024). Python. Accessed: Dec. 10, 2024. [Online]. Available: <https://github.com/BBillot/SynthSeg>
- [41] J. P. Dmochowski, A. Datta, M. Bikson, Y. Su, and L. C. Parra, “Optimized multi-electrode stimulation increases focality and intensity at target,” *J. Neural Eng.*, vol. 8, no. 4, p. 046011, Jun. 2011, doi: 10.1088/1741-2560/8/4/046011.
- [42] J. P. Dmochowski *et al.*, “Targeted transcranial direct current stimulation for rehabilitation after stroke,” *NeuroImage*, vol. 75, pp. 12–19, Jul. 2013, doi: 10.1016/j.neuroimage.2013.02.049.
- [43] Y. Huang, C. Thomas, A. Datta, and L. C. Parra, “Optimized tDCS for Targeting Multiple Brain Regions: An Integrated Implementation,” in *2018 40th Annual International Conference of the IEEE Engineering in Medicine and Biology Society (EMBC)*, Jul. 2018, pp. 3545–3548. doi: 10.1109/EMBC.2018.8513034.
- [44] Y. Zhang, M. Brady, and S. Smith, “Segmentation of brain MR images through a hidden Markov random field model and the expectation-maximization algorithm,” *IEEE Trans. Med. Imaging*, vol. 20, no. 1, pp. 45–57, Jan. 2001, doi: 10.1109/42.906424.
- [45] H. Wang and P. Yushkevich, “Multi-atlas segmentation with joint label fusion and corrective learning—an open source implementation,” *Front. Neuroinformatics*, vol. 7, Nov. 2013, doi: 10.3389/fninf.2013.00027.
- [46] B. Menze *et al.*, “The Multimodal Brain Tumor Image Segmentation Benchmark (BRATS),” *IEEE Trans. Med. Imaging*, vol. 34, no. 10, p. 1993, 2014, doi: 10.1109/TMI.2014.2377694.
- [47] E. Giacomello, D. Loiacono, and L. Mainardi, “Brain MRI Tumor Segmentation with Adversarial Networks,” in *2020 International Joint Conference on Neural Networks (IJCNN)*, Jul. 2020, pp. 1–8. doi: 10.1109/IJCNN48605.2020.9207220.
- [48] M. C. de Verdier *et al.*, “The 2024 Brain Tumor Segmentation (BraTS) Challenge: Glioma Segmentation on Post-treatment MRI,” May 28, 2024, *arXiv*: arXiv:2405.18368. doi: 10.48550/arXiv.2405.18368.
- [49] S. B. info@sagebase.org, “BraTS 2024.” Accessed: Dec. 27, 2024.

- [Online]. Available: <https://www.synapse.org/Synapse:syn53708249>
- [50] M. A. Mazurowski, M. Buda, A. Saha, and M. R. Bashir, "Deep learning in radiology: An overview of the concepts and a survey of the state of the art with focus on MRI," *J. Magn. Reson. Imaging*, vol. 49, no. 4, pp. 939–954, 2019, doi: 10.1002/jmri.26534.
- [51] A. S. Lundervold and A. Lundervold, "An overview of deep learning in medical imaging focusing on MRI," *Z. Für Med. Phys.*, vol. 29, no. 2, pp. 102–127, May 2019, doi: 10.1016/j.zemedi.2018.11.002.
- [52] "OSF | MICA-MICs: a dataset for Microstructure-Informed Connectomics." Accessed: Jan. 01, 2025. [Online]. Available: <https://osf.io/j532r/>
- [53] "Human Connectome Project (HCP) - National Institute of Mental Health (NIMH)." Accessed: Jan. 01, 2025. [Online]. Available: <https://www.nimh.nih.gov/research/research-funded-by-nimh/research-initiatives/human-connectome-project-hcp>
- [54] A. Klein *et al.*, "Mindboggling morphology of human brains," *PLOS Comput. Biol.*, vol. 13, no. 2, p. e1005350, Feb. 2017, doi: 10.1371/journal.pcbi.1005350.
- [55] R. C. Petersen *et al.*, "Alzheimer's Disease Neuroimaging Initiative (ADNI)," *Neurology*, vol. 74, no. 3, pp. 201–209, Jan. 2010, doi: 10.1212/WNL.0b013e3181cb3e25.
- [56] B. Fischl, "FreeSurfer," *NeuroImage*, vol. 62, no. 2, pp. 774–781, 2012, doi: 10.1016/j.neuroimage.2012.01.021.
- [57] C. Team, "Catalyst.Neuro: A 3D Brain Segmentation Pipeline for MRI," PyTorch. Accessed: Dec. 25, 2024. [Online]. Available: <https://medium.com/pytorch/catalyst-neuro-a-3d-brain-segmentation-pipeline-for-mri-b1bb1109276a>
- [58] A. Fedorov, E. Damaraju, V. Calhoun, and S. Plis, "Almost instant brain atlas segmentation for large-scale studies," Nov. 01, 2017, *arXiv: arXiv:1711.00457*. doi: 10.48550/arXiv.1711.00457.
- [59] A. Fedorov, J. Johnson, E. Damaraju, A. Ozerin, V. Calhoun, and S. Plis, "End-to-end learning of brain tissue segmentation from imperfect labeling," Jun. 05, 2017, *arXiv: arXiv:1612.00940*. doi: 10.48550/arXiv.1612.00940.
- [60] "Connectome - Homepage." Accessed: Jan. 01, 2025. [Online]. Available: <https://www.humanconnectome.org/>
- [61] mailto:arno@binarybottle.com, "Mindboggle." Accessed: Jan. 01, 2025. [Online]. Available: <https://mindboggle.info/data>
- [62] B. Billot, C. Magdamo, Y. Cheng, S. E. Arnold, S. Das, and J. E. Iglesias, "Robust machine learning segmentation for large-scale analysis of heterogeneous clinical brain MRI datasets," *Proc. Natl. Acad. Sci.*, vol. 120, no. 9, p. e2216399120, Feb. 2023, doi: 10.1073/pnas.2216399120.
- [63] "Alzheimer's Disease Neuroimaging Initiative," ADNI. Accessed: Jan. 01, 2025. [Online]. Available: <https://adni-ide.loni.usc.edu/>
- [64] B. Fischl *et al.*, "Whole Brain Segmentation: Automated Labeling of Neuroanatomical Structures in the Human Brain," *Neuron*, vol. 33, no. 3, pp. 341–355, Jan. 2002, doi: 10.1016/S0896-6273(02)00569-X.
- [65] O. Puonti, J. E. Iglesias, and K. Van Leemput, "Fast and sequence-adaptive whole-brain segmentation using parametric Bayesian modeling," *NeuroImage*, vol. 143, pp. 235–249, Dec. 2016, doi: 10.1016/j.neuroimage.2016.09.011.
- [66] "Generalizing Deep Learning for Medical Image Segmentation to Unseen Domains via Deep Stacked Transformation." Accessed: Dec. 27, 2024. [Online]. Available: <https://xplore.staging.ieee.org/document/8995481?denied=>
- [67] F. Isensee, P. F. Jaeger, S. A. A. Kohl, J. Petersen, and K. H. Maier-Hein, "nnU-Net: a self-configuring method for deep learning-based biomedical image segmentation," *Nat. Methods*, vol. 18, no. 2, pp. 203–211, Feb. 2021, doi: 10.1038/s41592-020-01008-z.
- [68] "(PDF) Extending nn-UNet for Brain Tumor Segmentation," *ResearchGate*, Nov. 2024, doi: 10.1007/978-3-031-09002-8_16.
- [69] A. Hatamizadeh, V. Nath, Y. Tang, D. Yang, H. Roth, and D. Xu, "Swin UNETR: Swin Transformers for Semantic Segmentation of Brain Tumors in MRI Images," Jan. 04, 2022, *arXiv: arXiv:2201.01266*. doi: 10.48550/arXiv.2201.01266.
- [70] lkshrsch, *lkshrsch/multiaxial_brain_segmeneter*. (Dec. 05, 2024). Python. Accessed: Jan. 13, 2025. [Online]. Available: https://github.com/lkshrsch/multiaxial_brain_segmeneter